Research Article | Open Access

Microstructures

Tang *et al. Microstructures* **2026**, *6*, 2026072 **DOI:**10.20517/microstructures.2025.184

Thermally tailored cellular microstructure enhances ductility in additively manufactured maraging steel via austenite network reconstruction

Junjie Tang[1], Yishuang Yu[1], Zhihui Xiong[2], Shilong Liu[1], R.D.K. Misra[3], Xuejun Jin[1,2]

Keywords:
Additive manufacturing, laser powder bed fusion, maraging steel, cellular microstructure, austenite stability, transformation-induced plasticity

Citation: Tang, J.; Yu, Y.; Xiong, Z.; Liu, S.; Misra, R.; Jin, X. Thermally tailored cellular microstructure enhances ductility in additively manufactured maraging steel via austenite network reconstruction. *Microstructures* **2026**, *6*, 2026072. https://dx.doi.org/10.20517/microstructures.2025.184

Received: 31 Dec 2025 **First Decision:** 30 Jan 2026 **Revised:** 14 Feb 2026 **Accepted:** 10 Mar 2026 **Published:** 29 May 2026

Academic Editors: Wen Chen, Nima Haghdadi **Copy Editor:** Ping Zhang **Production Editor:** Ping Zhang

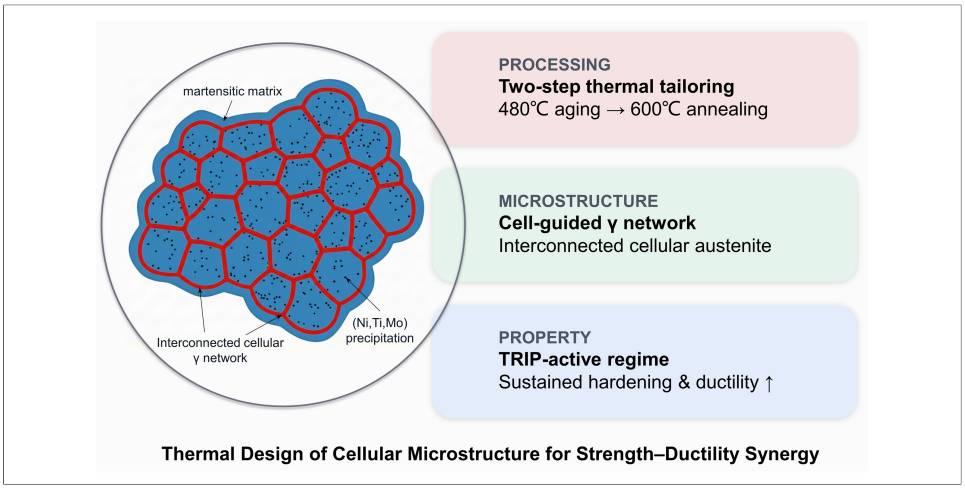

Abstract

Overcoming the strength-ductility trade-off remains a challenge for both traditional and emerging high-strength steels. The unique thermal history during additive manufacturing (AM) of metals and alloys includes cellular solute enrichment of alloying elements, enabling the formation of metastable austenite with a cellular morphology after intercritical ($\alpha + \gamma$) annealing. Intercritical heat treatment reconstructs the trace retained austenite in the as-printed microstructure, together with reverted austenite from the martensitic matrix, into an interconnected cellular austenite network (~40 vol.%). Yet solute-gradient partitioning can over-stabilize this cellular austenite, suppressing transformation-induced plasticity (TRIP) and work hardening under room-temperature tensile straining and making its stability difficult to tune using conventional heat-treatment schedules. Here, we effectively tune the thermal stability of cellular austenite in laser powder bed fusion (L-PBF) 18Ni300 maraging steel through a multi-step intercritical annealing strategy, so that TRIP can be readily activated during room-temperature tensile loading. Serial *ex-situ*

[1]Institute of Advanced Steels and Materials, School of Materials Science and Engineering, Shanghai Jiao Tong University, Shanghai 200240, China.
[2]Institute of Medical Robotics, School of Biomedical Engineering, Shanghai Jiao Tong University, Shanghai 200240, China.
[3]Interdisciplinary Structural and Functional Materials Science and Engineering Research Group, Department of Biomedical Engineering and Department of Mechanical, Robotics and Industrial Engineering, Lawrence Technological University, Southfield, MI 48075, USA.

Correspondence to: Prof. Xuejun Jin, School of Materials Science and Engineering and School of Biomedical Engineering, Shanghai Jiao Tong University, Shanghai 200240, China. E-mail: jin@sjtu.edu.cn; Prof. Shilong Liu, School of Materials Science and Engineering, Shanghai Jiao Tong University, Shanghai 200240, China. E-mail: sliu6@sjtu.edu.cn; Prof. Zhihui Xiong, School of Biomedical Engineering, Shanghai Jiao Tong University, Shanghai 200240, China. E-mail: xiongzhihui@sjtu.edu.cn

electron backscatter diffraction (EBSD)/X-ray diffraction (XRD) measurements at comparable locations indicated a substantially larger austenite-to-martensite ($\gamma \rightarrow \alpha'$) transformation (41.5% → 22.3%) as compared to the conventional single-step annealed counterpart (37.7% → 28.1%), consistent with an earlier TRIP onset. Consequently, the optimized condition exhibits significantly enhanced ductility and an extended uniform work-hardening regime (over 50% improvement), attributable to the reduced stability of reverted austenite, which facilitates earlier and more extensive strain-induced $\gamma \rightarrow \alpha'$ transformation. Finally, we propose a microstructure design concept of "cellular structure - retained austenite - cellular austenite network" for strength - ductility synergy, providing a transferable paradigm for strengthening and toughening of other AM metals.

INTRODUCTION

Metal additive manufacturing (AM) technique, as an advanced processing method, has already arisen a heated debate over the past decade. Compared with conventional subtractive manufacturing (milling, grinding, lathing, *etc.*), metal AM features high processing accuracy, instant forming speed and customized design freedom[1-3]. As such, metal AM products are seeing increasing adoption in aerospace, energy and biomedical industries where excellent mechanical performance is required[4-6].

To meet the critical demand for strength and ductility, maraging steels (represented by several high-Ni series like 18Ni300) are among the most widely deployed materials. During aging, enrichment of alloying elements facilitates precipitation hardening and elevates maximum tensile strength to over 2 GPa, while ductility is often compromised. The nonideal strength-ductility combination restricts the broader application of conventional maraging steels, partly due to the low fraction and constrained morphology of retained austenite, which typically remains below 5 vol.% (phase volume fraction) and appears as plate- or thin-film morphologies after heat treatment[7,8]. Although there were attempts to utilize retained austenite as a triggering phase to improve ductility, the effectiveness is frequently limited by its low fraction, constrained morphology, and the rapid exhaustion of transformation-induced plasticity (TRIP) during deformation[9-11].

Unlike wrought maraging steels, laser powder bed fusion (L-PBF) processing involves rapid solidification and cyclic reheating, leading to hierarchical substructures and pronounced micro-segregation at cell boundaries[12-14]. While such chemical heterogeneity is commonly homogenized by solid-solution heat-treatment, several studies indicate that the as-printed cellular segregation can be leveraged as a "chemical template" to promote austenite reversion along cell boundaries and modify mechanical behavior[15-18]. For example, prior studies have demonstrated that cellular microstructures can accelerate austenite reversion along cell boundaries during aging[19-21]. Nevertheless, how to tailor the stability of the reverted austenite in such cellular AM microstructures remains challenging[22].

This challenge arises because cellular austenite formation in AM maraging steels introduces a stability dilemma[23]. The same solute gradients that enable preferential austenite reversion along cell boundaries can also over-stabilize the reverted austenite, thereby suppressing $\gamma \rightarrow \alpha'$ transformation and reducing TRIP activity at room-temperature tensile loading[24,25]. Consequently, heat-treatment strategies that work for tuning reverted austenite in more homogeneous microstructures may be less effective for AM maraging steels, where precipitation and austenite reversion are strongly coupled and governed by spatially heterogeneous solute partitioning[26,27].

A further complication is the competition between precipitation strengthening and austenite stabilization[28,29]. Alloying elements that drive precipitation during aging also influence austenite reversion kinetics and austenite stability; thus, maximizing precipitation strengthening can inadvertently lock the reverted austenite into an over-stable state[30-32]. Conversely, promoting austenite reversion may compromise

peak strength. Recent work on AM maraging steels has highlighted these coupled phenomena (cellular structure evolution, precipitation sequence, austenite reversion and their impacts on strength-ductility performance), underscoring the need for thermal pathways that can coordinate these effects[33,34].

Despite the growing recognition that cellular segregation can promote reverted austenite formation in L-PBF maraging steels, it remains unclear how to deliberately tune the stability of cellular austenite so that TRIP is reliably activated at room temperature without sacrificing precipitation strengthening. Here, we design a multi-step intercritical annealing route for L-PBF 18Ni300 that leverages the as-printed cellular structure to reconstruct a high-fraction (~40 vol.%) interconnected cellular austenite network, and then intentionally adjusts its stability to enable TRIP activation during room-temperature tension. The selected temperatures were chosen to balance precipitation strengthening and austenite reversion: 480 °C is a widely reported peak-aging condition for 18Ni300 maraging steel, whereas 600 °C lies within the α' + γ intercritical region to enable controlled austenite reversion. By correlating serial *ex-situ* microstructure tracking with deformation-induced phase transformation, we establish a structure - property linkage and propose a "cellular structure - retained austenite - cellular austenite network" design concept for strength - ductility synergy, offering guidance for strengthening and toughening strategies in other AM alloys that inherit cellular segregation.

MATERIALS AND METHODS

Material and L-PBF processing

Gas-atomized 18Ni300 maraging steel powder (sieved particle-size range: 15~53 μm) with generally spherical morphology and a nominal composition of Fe-17.78Ni-8.99Co-4.74Mo-0.74Ti (wt.%) was used in this study. All specimens were fabricated on an HBD-80 L-PBF system (Guangdong Hanbang Laser Technology Co., Ltd., China), also commonly referred to as selective laser melting (SLM), under a nitrogen atmosphere with continuous gas circulation and oxygen level maintained below 1,000 ppm. The primary processing parameters were: laser power 180 W, scanning speed 1,200 mm/s, hatch spacing 0.05 mm, layer thickness 30 μm, and a fiber-laser spot diameter of 0.09 mm. A soft-blade recoater was used, with other recoating settings following the machine default parameters. A chessboard scanning strategy was adopted with a typical island size of 5 × 5 mm^2 and a 67° rotation between successive layers. The build plate was not preheated (room temperature). For tensile specimens, the build direction (BD) was perpendicular to the tensile axis (BD ⊥ tensile axis). After fabrication, the specimens were removed from the build plate and machined into flat dog-bone tensile coupons (gauge length 15 mm, width 4.5 mm and thickness 1.5 mm).

Heat treatment

Post-processing heat treatments were designed to reconstruct a metastable reverted austenite network and to tailor its stability[8,34-36]. The investigated conditions included: (i) as-printed; (ii) T-480, aging at 480 °C for 3 h; (iii) L-600, intercritical dual-phase (α + γ) annealing at 600 °C for 1 h; and (iv) TL-480-600, a two-step route consisting of 480 °C aging for 3 h followed by intercritical annealing at 600 °C for 1 h. All heat treatments were carried out in a muffle furnace (Nabertherm, Germany; model P330) under air atmosphere (hot-furnace insertion; estimated to take a few minutes for the specimens to reach temperature, corresponding to an effective heating rate on the order of 10^2 °C min^{-1}). The furnace temperature was calibrated using an external thermocouple placed adjacent to the specimens (the setpoint temperature was verified prior to heat treatment). After each step, specimens were water-quenched to room temperature (estimated cooling rate of 10^2 °C s^{-1}).

Microstructure characterization

Scanning electron microscopy (SEM) observations were performed on small blocks cut from the grip sections of tensile specimens. Samples were hot mounted, ground and polished, followed by etching with 4 vol.% nital for 40 s. Microstructures were examined using a JSM-7800F field-emission SEM (JEOL, Japan)

operated at 5 kV (working distance ~10 mm).

Transmission electron microscopy (TEM) foils were prepared from 400-μm-thick wafers sectioned from the grip region, followed by mechanical thinning. Discs (3 mm diameter) were electropolished to electron transparency using a TenuPol-5 twin-jet electropolisher (Struers, Denmark) with 7 vol.% perchloric acid at 50 V for 70 s. TEM examinations were carried out on a Talos F2000X G2 microscope (Thermo Fisher Scientific, USA) operated at 200 kV. TEM energy-dispersive X-ray spectroscopy (TEM-EDS) maps were acquired using a 512 × 512 pixel grid over a view field of ~0.5 μm (pixel size ~1.0 nm/pixel) with a total acquisition time of ~10 min per map.

X-ray diffraction (XRD) was used to identify phases and quantify γ fraction. To ensure surface flatness, the bulk specimens (cubes, with a single length of 5 mm) were ground and electropolished using 7 vol.% perchloric acid at 25 V for ~30 s. XRD scans were conducted on a D8 multifunctional diffractometer (Bruker, Germany) using Cu-Kα radiation (λ = 0.154 nm) in Bragg-Brentano geometry over 2θ = 40° - 100° at 2°/min. The γ volume fraction was calculated following the standard approach for austenite quantification in steels, using an integrated-intensity method based on multiple face-centered cubic (FCC) and body-centered cubic (BCC) reflections to ensure reliable phase fraction by minimizing peak-overlap and single-peak bias. Specifically, the integrated intensities of $(200)_{\gamma}$, $(200)_{\alpha'}$, $(220)_{\gamma}$, $(211)_{\alpha'}$ and $(311)_{\gamma}$ peaks were used, as these reflections are strong and relatively well separated in the selected 2θ range, reducing uncertainty associated with any single peak. No explicit texture or absorption correction was applied. Instead, the multi-peak approach together with the adopted surface preparation was used to minimize texture-related bias.

Electron backscatter diffraction (EBSD) was performed on a GAIA3 GMU SEM (TESCAN, Czech Republic; model 2016) at an accelerating voltage of 20 kV, with the specimen tilted at 70° and a working distance of ~10 mm. The surface preparation procedures were identical to those for XRD. EBSD maps were acquired at a magnification of 3000×, using a step size of 0.12 μm (approximately one-tenth of the characteristic cellular structure size) over a typical scanned area of 120 × 90 μm^2. The detector acquisition settings were fixed across all conditions (gain = 6, exposure time = 25 ms) to ensure data comparability. Typical indexing rates (fraction of indexed points) were > 90%, and the remaining non-indexed pixels were handled during post-processing as described below. Phase indexing and map reconstruction were carried out in AZtecCrystal (Oxford Instruments, UK), and a consistent post-processing workflow was applied, including: (i) removal of non-indexed pixels based on a confidence threshold; (ii) wild-peak reduction using neighbor correlation; and (iii) grain dilation to improve phase-boundary continuity while preserving fine cellular features. To track strain-induced martensitic transformation, serial *ex-situ* EBSD mapping was conducted on tensile specimens interrupted at engineering strains of 0%, 2.5%, and 5.0%, as well as after fracture. To ensure comparability across strain states, EBSD maps were acquired from cross-sections prepared at comparable locations (i.e., the same distance from the fracture surface)[37].

Mechanical testing

Uniaxial tensile tests were conducted at room temperature following GB/T 228.1-2010 using a Z100 TEW universal testing machine (ZwickRoell, Germany) equipped with the built-in 15-mm extensometer at a constant crosshead speed of 0.01 mm/s throughout the entire test (corresponding to a nominal strain rate of 6.7×10^{-4} s^{-1}). At least three specimens were tested for each condition. The work of fracture (WOF) was obtained by numerically integrating the engineering stress-strain curve up to fracture. For consistency with the Ashby map, WOF is reported in MPa·% with engineering strain expressed in percent. For strain-hardening analysis, engineering stress–strain data were converted to true stress-strain up to the onset necking. The instantaneous strain-hardening exponent was calculated as $n = (d \ln\sigma_{true}/d \ln\varepsilon_{true})$ using a backward finite-difference scheme (after smoothing the true stress-strain data), and plotted as a function of

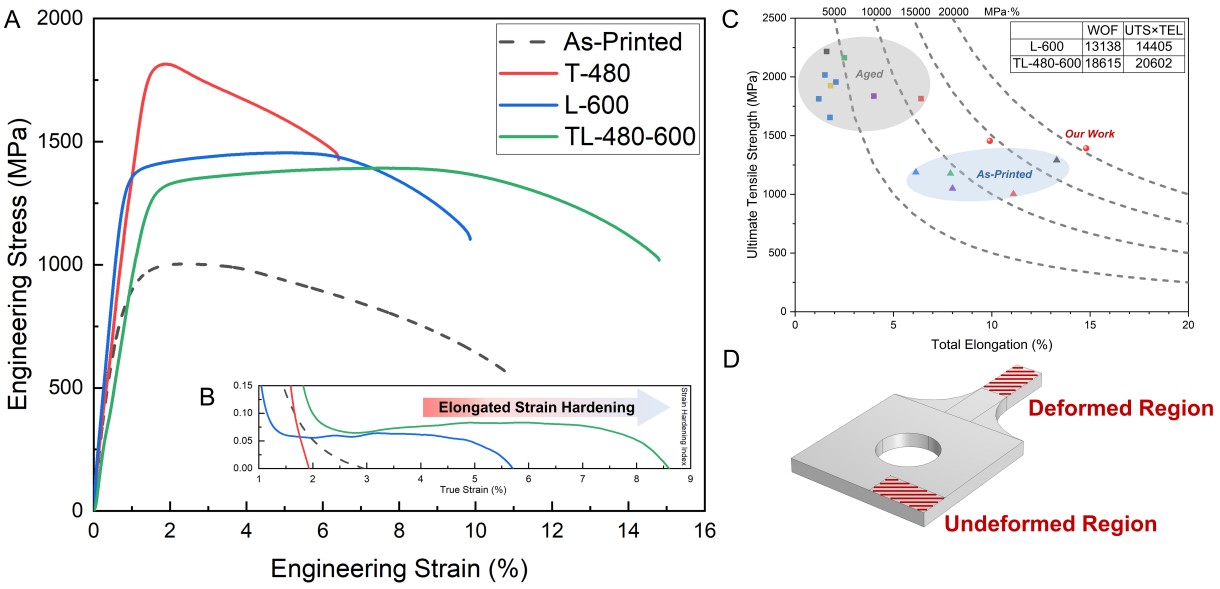

Figure 1. Room-temperature tensile behavior of L-PBF 18Ni300 under different heat-treatment routes: (A) Engineering stress-strain curves for the as-printed, T-480, L-600, and TL-480-600 conditions; (B) Strain hardening behavior quantified by the instantaneous strain-hardening exponent, plotted as a function of true strain. The derivative was evaluated using a backward-difference scheme based on the true stress-strain data after a light smoothing; (C) Ashby strength-ductility map (UTS *vs.* TEL) for the investigated conditions and selected literature data[9,38-42]. Triangles, squares, and red circles denote as-printed literature data, aged literature data, and the present work, respectively. Marker colors are used to distinguish different literature sources. Dashed contours denote constant strength-ductility product (UTS × TEL); (D) Schematic of the tensile specimen indicating the gauge (deformed) and grip (undeformed) regions used for microstructural characterization. L-PBF: Laser powder bed fusion; WOF: work of fracture; UTS: ultimate tensile strength; TEL: total elongation.

true strain.

RESULTS AND DISCUSSION

Overview of microstructural evolution and mechanical behavior

Figure 1 and Table 1 provide an overview of the room-temperature tensile behavior of L-PBF 18Ni300 under four conditions (as-printed, T-480, L-600 and TL-480-600), together with their strain-hardening characteristics and the corresponding strength-ductility map (Ashby plots). Figure 1A shows representative engineering stress-strain curves for each condition, whereas Table 1 summarizes the corresponding tensile properties as mean ± standard deviation (based on replicate tests for each condition). From the curves in Figure 1A, the as-printed alloy exhibits moderate strength and ductility [yield strength (YS) = 792 MPa, ultimate tensile strength (UTS) = 997 MPa, uniform elongation (UEL) = 2.4%, total elongation (TEL) = 10.8%] with a low retained austenite fraction ($\gamma \approx 3.1\%$). Aging at 480 °C for 3 h (T-480) produces a strong precipitation-hardened response, leading to the highest strength (YS = 1,823 MPa, UTS = 1,862 MPa), but at the expense of ductility (UEL = 1.8%, TEL = 6.7%) despite a slightly increased γ fraction (≈ 6.8%). In contrast, intercritical annealing at 600 °C for 1 h (L-600) results in a high reverted austenite fraction ($\gamma \approx 37.7\%$) and improves uniform deformation (UEL = 4.7%, TEL = 9.7%) while maintaining high strength (YS = 1,320 MPa, UTS = 1,428 MPa). Most notably, the two-step route (TL-480-600) reconstructs an even higher γ fraction (≈ 41.5%) and achieves the best strength-ductility synergy (YS = 1,275 MPa, UTS = 1,381 MPa, UEL = 7.6%, TEL = 14.6%), indicating a substantially enhanced capability to sustain uniform plastic flow.

The strain-hardening response further rationalizes the ductility differences. The strain-hardening behavior is quantified by the instantaneous strain-hardening exponent n, as summarized in Figure 1B. In the early plastic regime, both L-600 and TL-480-600 show a rapid drop in n, which is typical of the transient

Table 1. Room-temperature tensile properties and austenite volume fraction of L-PBF 18Ni300

Condition	Heat treatment	γ (vol.%)	YS (MPa)	UTS (MPa)	UEL (%)	TEL (%)
As-printed	-	3.1	792 ± 18	997 ± 22	2.4 ± 0.2	10.8 ± 0.7
T-480	480/3 h	6.8	1,823 ± 61	1,862 ± 55	1.8 ± 0.2	6.7 ± 0.5
L-600	600/1 h	37.7	1,320 ± 37	1,428 ± 46	4.7 ± 0.4	9.7 ± 0.6
TL-480-600	480/3 h + 600/1 h	41.5	1,275 ± 41	1,381 ± 27	7.6 ± 0.8	14.6 ± 1.1

γ, austenite volume fraction (retained in as-printed, reverted after intercritical annealing). YS: Yield strength; UTS: ultimate tensile strength; UEL: uniform elongation; TEL: total elongation.

hardening immediately after yielding. A clear divergence then develops: TL-480-600 maintains an extended, relatively stable *n*-plateau over a broad strain interval, whereas L-600 exhibits a lower plateau followed by an earlier decay of *n*. In the late stage, *n* in L-600 approaches zero at a much smaller true strain, indicative of earlier strain localization and a shortened uniform-deformation window, while TL-480-600 sustains positive strain hardening to larger strains, consistent with its higher UEL and TEL [Figure 1A and Table 1]. To provide a holistic comparison of energy absorption beyond point metrics, we further quantify the WOF by integrating the engineering stress-strain curves, and benchmark it together with the strength-ductility product, UTS×TEL, in the Ashby map [Figure 1C]. The Ashby plot highlights that the present design shifts the performance envelope from the aged "high-strength-low-ductility" domain toward an improved synergy region, comparing favorably with the as-printed and conventionally annealed counterparts[43]. Consistent with the more persistent strain hardening of TL-480-600, its work of fracture and UTS×TEL are both markedly higher than those of L-600 (by 40% for WOF and 43% for UTS×TEL), indicating improved energy-absorption capability over the entire deformation process. Importantly, this enhanced and prolonged hardening is consistent with an earlier TRIP activation, which will be further evidenced by serial *ex-situ* EBSD mapping and XRD quantification (see Figure 1D for specimen geometry). Moreover, significant prior austenite grain coarsening typically occurs during high-temperature homogenization, while the present 480 and 600 °C treatments are below this regime and thus are not expected to induce pronounced grain growth.

These macroscopic signatures indicate that the optimized route enables (i) earlier activation of transformation-assisted hardening and (ii) a longer-lasting barrier-controlled hardening regime dominated by precipitation and cell boundaries. Accordingly, the following sections establish a microstructure-property linkage through a continuous evidence chain, starting from the as-printed cellular template, to austenite reconstruction into a cellular network, to precipitation and stability tuning for room-temperature TRIP, and ultimately to an integrated strengthening-toughening design.

As-printed cellular template retained through heat treatment

Figure 2 compares the representative SEM micrographs of as-printed and heat-treated L-PBF 18Ni300, illustrating how the as-printed cellular template is preserved or modified by different thermal routes. Here, the term "cellular template" refers to the as-printed cellular substructure and the associated solute-segregated cell walls formed during L-PBF (together with any trace retained austenite present in the as-printed state). In the as-printed condition [Figure 2A], a well-defined honeycomb-like cellular network is clearly visible, providing a topological framework that can guide subsequent phase reversion and microstructure reconstruction.

Post heat treatment alters the visibility and continuity of the cellular framework in a route-dependent manner. After aging at 480 °C (T-480), the cellular contrast becomes weaker but remnants of the cellular structure remain detectable (Figure 2B, white arrows), indicating that aging primarily promotes precipitation strengthening while only partially smoothing the solute-segregation-defined cell walls. A scale-bar-calibrated

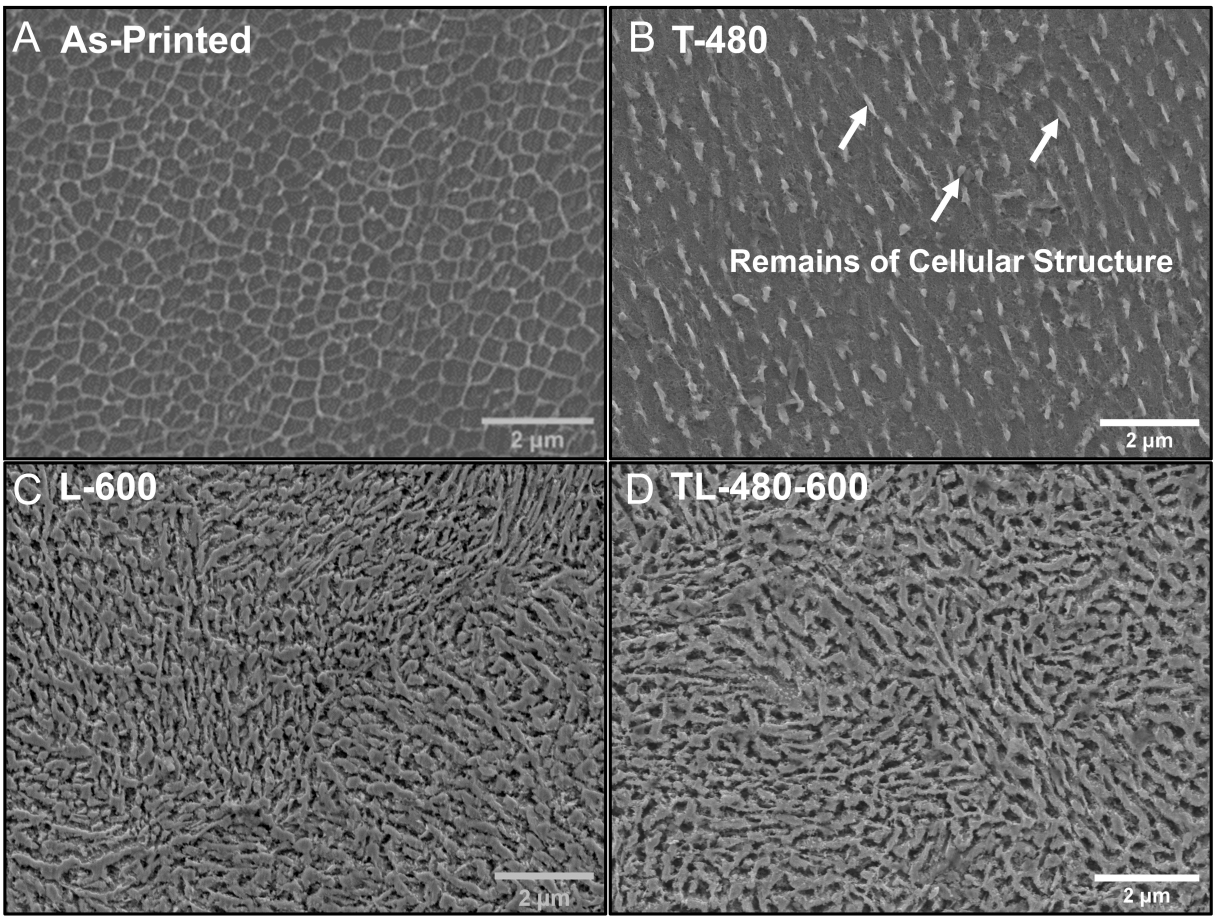

Figure 2. SEM micrographs showing the evolution of the as-printed cellular substructure after heat-treatment in L-PBF 18Ni300: (A) As-printed; (B) T-480; (C) L-600; (D) TL-480-600. White arrows in (B) mark residual cellular features. Scale bars as indicated. L-PBF: Laser powder bed fusion; SEM: scanning electron microscopy.

estimate from Figure 2 suggests that the characteristic spacings are of the same order of magnitude; the as-printed cellular network shows a typical spacing of 0.6~0.7 μm, whereas the discernible cellular remnants in T-480 exhibit an apparent spacing of 1.0~1.2 μm, likely reflecting partial dissolution of the cellular features during aging and thus a slightly sparser population of visible traces. In contrast, after single-step intercritical annealing at 600 °C (L-600), the microstructure evolves into a more recovered appearance and the original cellular network becomes much less discernible [Figure 2C], suggesting a stronger tendency for dissolution and redistribution of the as-printed cellular heterogeneity. Notably, the two-step route (TL-480-600) retains a higher degree of microstructural heterogeneity and preserves identifiable cellular traces within the transformed matrix [Figure 2D], consistent with the concept that the initial aging step can "lock in" part of the cellular framework and thereby provide a more persistent scaffold during the subsequent intercritical annealing.

This observation is important for the present design strategy: rather than eliminating the AM-inherited cellular segregation, the optimized heat treatment aims to retain sufficient cellular template features to promote network-connected austenite reconstruction, while allowing controlled redistribution of solutes and precipitation to tune austenite stability for room-temperature TRIP activation[44]. It should be noted that the etched SEM contrast primarily reflects the persistence and redistribution of cellular framework and defect-rich boundaries, whereas the phase constitution is further identified by EBSD, XRD, and TEM in the following sections.

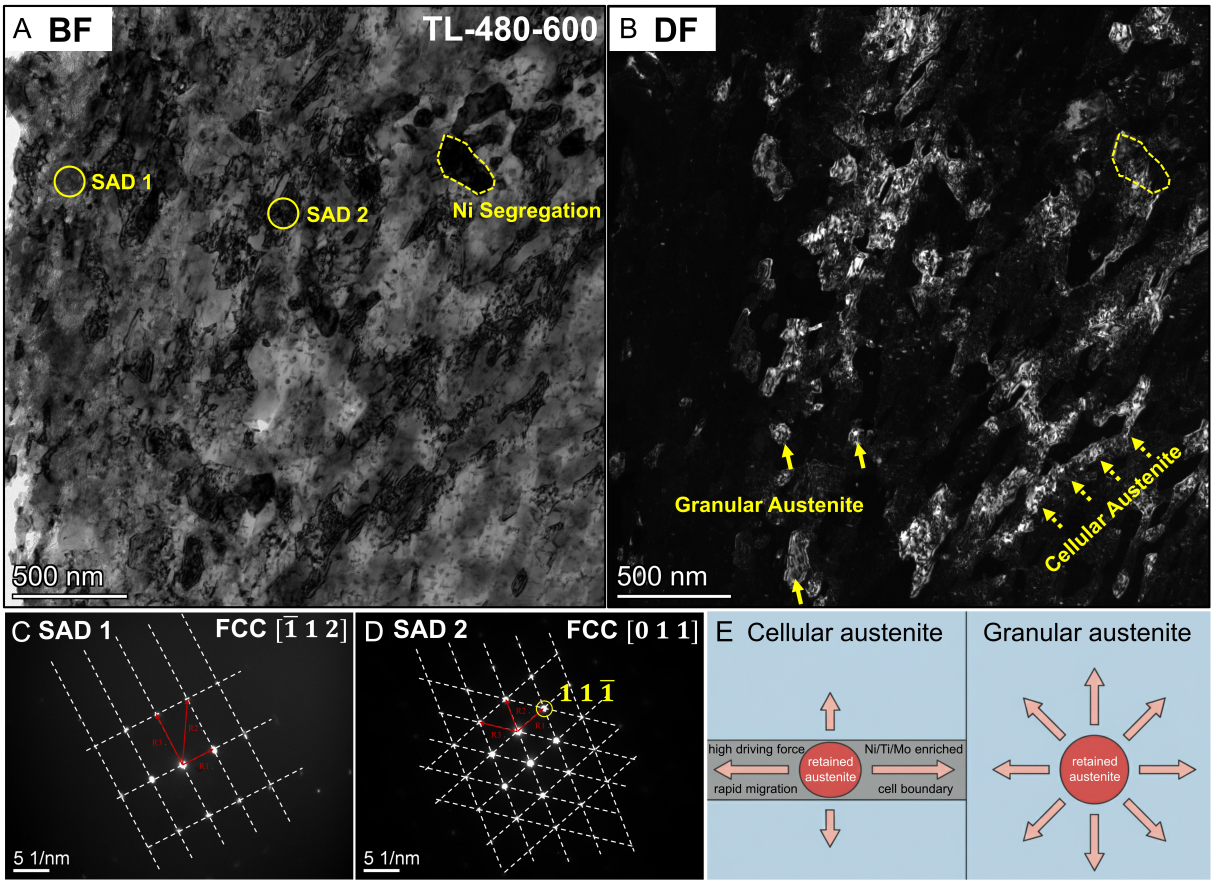

Figure 3. TEM evidence for reverted-austenite morphologies reconstructed in TL-480-600: (A) Bright-field (BF) image with a Ni-segregated region outlined; regions for SAD are marked; (B) Dark-field (DF) image highlighting austenite-containing regions, including interconnected cellular austenite (dotted arrows) and granular austenite (solid arrows); (C and D) SAD patterns acquired from the marked regions; (E) Schematic illustration of segregation-guided austenite growth relative to the cellular template, where arrow length qualitatively indicates the relative local driving force for the depicted migration process, inspired by the concept in Ref.[19]. SAD: Selected-area diffraction; TEM: transmission electron microscopy; FCC: face-centered cubic.

Austenite reconstruction: morphology, fraction and network connectivity

Figure 3 provides direct evidence that the reverted austenite formed in TL-480-600 is not morphologically uniform, but develops through two distinct growth modes that are intrinsically linked to the AM-inherited cellular segregation template. The bright-field (BF) image [Figure 3A] shows a heterogeneous matrix with localized Ni-segregated regions, while the dark-field (DF) image [Figure 3B] highlights austenite-containing domains with two representative morphologies: (i) cellular austenite distributed along elongated, interconnected cell boundaries, and (ii) granular austenite appearing as discrete bright particles. Selected-area diffraction (SAD) patterns [Figure 3C and D] confirm the FCC structure of the reverted austenite, supporting that the bright contrast in DF imaging corresponds to austenite rather than non-austenitic second phases. Importantly, the spatial position of the Ni-segregation region coincides with the austenite-enriched domain, indicating that chemical heterogeneity inherited from L-PBF strongly dictates where austenite nucleates and how it grows, rather than producing a random distribution.

To rationalize the two morphologies observed in the DF image [Figure 3B], we attribute their formation to both thermodynamic factors (local γ stabilization) and kinetic factors (pathway-controlled growth) under AM non-equilibrium conditions. In L-PBF, rapid solidification with limited back-diffusion (i.e., insufficient time for solute redistribution in the solid state to homogenize segregation) creates a solute-segregated cellular template, producing a spatially heterogeneous chemical-potential landscape. Local enrichment of γ

-stabilizing solutes (primarily Ni, associated with Ti/Mo) increases the driving force for γ reversion and depresses the martensitic transformation temperature (Ms), enabling reverted γ to form and persist in enriched zones. Meanwhile, the cyclic L-PBF thermal history (rapid cooling followed by repeated short-time reheating) promotes solute redistribution over short diffusion lengths and facilitates interfacial migration. Since cellular boundaries are defect-rich and commonly solute-decorated, they provide fast diffusion paths and a contiguous low-resistance network, along which γ reversion can propagate more readily than through the cell interiors[19]. As a result, γ growth tends to follow the cellular boundary network, giving rise to an interconnected cellular morphology.

Under this framework, whether reverted γ develops into an interconnected cellular network or discrete granular islands depends not only on the presence of enrichment, but also on how that enrichment is distributed geometrically. When enrichment is boundary-confined and spatially continuous along the cellular network, the thermodynamic driving force is directionally biased along cell walls, favoring guided interface migration and thus cellular γ growth that inherits the topology of the as-printed template (schematically illustrated in Figure 3E, left). In contrast, when enrichment becomes locally concentrated into Ni-rich clusters without a continuous boundary pathway, γ is thermodynamically stabilized within localized regions and tends to grow more isotropically into granular islands, as its interface migration is not guided by a continuous boundary network and is therefore less directionally constrained (Figure 3E, right). Notably, this granular morphology is consistent with the blocky reverted austenite often reported in conventionally heat-treated maraging steels, in which locally stabilized γ grows more equiaxed when growth is not constrained by a continuous boundary pathway. Owing to the inherent spatial heterogeneity in composition and thermal history in AM, both growth modes can coexist within the same heat-treated specimen.

In summary, Figure 3 establishes that austenite reconstruction in TL-480-600 is a segregation-guided process, where the cellular solute template governs not only the amount of austenite formed but also its topology (cellular network *vs.* granular islands). This distinction is crucial for the subsequent stability tailoring and room-temperature TRIP activation.

Decoupling precipitation from austenite stability tailoring

A critical challenge in L-PBF 18Ni300 is that precipitation strengthening and austenite stability are intrinsically coupled through solute partitioning: the same alloying elements that promote nanoscale precipitates also participate in stabilizing reverted austenite along the AM-inherited cellular segregation template. Therefore, achieving strength-ductility synergy requires a thermal path that helps to decouple these two effects, i.e., retaining strong precipitation hardening while deliberately tuning (and when necessary weakening) the stability of cellular reverted austenite to enable room-temperature TRIP.

Figure 4 compares the precipitation state and local partitioning behavior in the single-step intercritical condition (L-600, Figure 4A-D) and the optimized two-step route (TL-480-600, Figure 4E-H). Given the limited spatial resolution of SEM-EDS for nanoscale features, we employ TEM-EDS mapping to visualize relative solute partitioning. The maps are interpreted in a semi-quantitative sense (intensity contrast) rather than as calibrated compositions. In both conditions, the Ni maps show discernible Ni-enriched regions, indicating that the L-PBF-induced chemical heterogeneity is not fully erased and can continue to serve as a template for austenite reversion. However, the extent of solute consumption by precipitation and the resulting interface chemistry differ markedly. In L-600, the precipitate population is comparatively sparse; Mo enrichment appears only in a limited number of particles, and the Ti signal is relatively weak and diffuse at this scale, suggesting that a larger fraction of solutes remains available to stabilize reverted austenite. This local chemical state is consistent with an over-stabilized austenite that is difficult to transform under room-temperature loading.

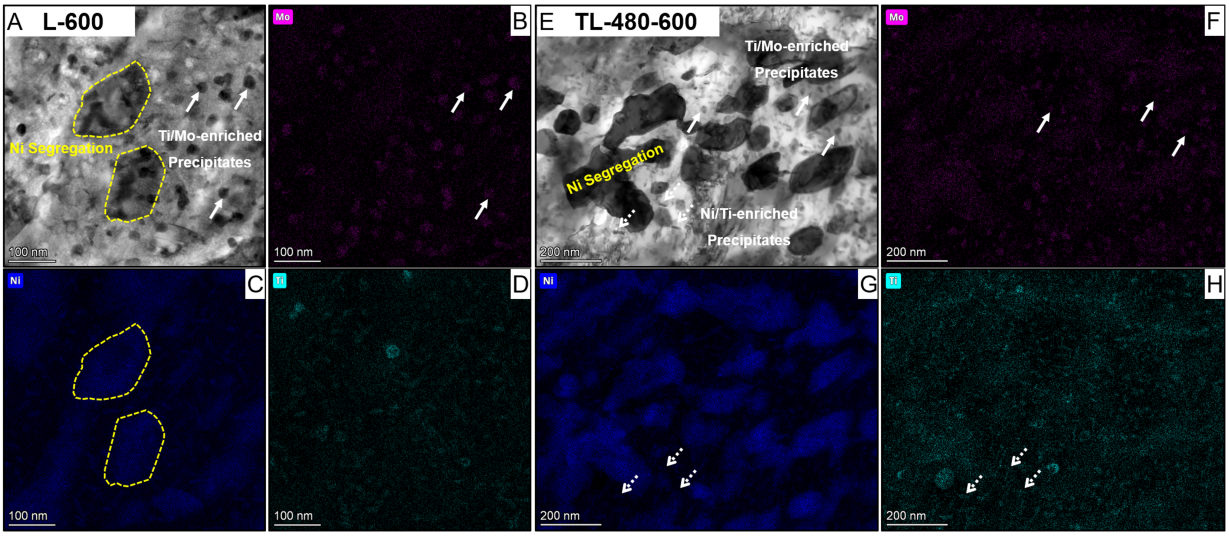

Figure 4. TEM-EDS evidence for precipitation and partitioning features in L-600 and TL-480-600: (A) L-600 electron micrograph; (B) Mo map, (C) Ni map, and (D) Ti map corresponding to (A); (E) TL-480-600 electron micrograph; (F) Mo map, (G) Ni map, and (H) Ti map corresponding to (E). Ni-enriched regions are outlined and Mo/Ti-enriched regions are marked by arrows. Scale bars as indicated. TEM-EDS: Transmission electron microscopy-energy-dispersive X-ray spectroscopy.

In contrast, TL-480-600 exhibits a much more pronounced precipitation signature. The Ni/Ti maps display clearer solute partitioning into precipitates (dotted arrows), implying high density of precipitation during the pre-aging plus annealing sequence. This intensified precipitation not only strengthens the matrix but also reshapes the solute reservoir at and near cellular interfaces that governs reverted-austenite stability. In other words, the pre-aging stage "pre-consumes" part of key alloying elements into precipitates, and the subsequent intercritical step reconstructs austenite under a modified local chemical environment. This sequencing provides a practical route to decouple precipitation from stability control: precipitation strengthening is secured, while the reverted/cellular austenite is prevented from entering an excessively stable state.

Considering the above, Figure 4 supports the core design logic of this work: the multi-step intercritical strategy is not aimed at maximizing austenite fraction per se, but at producing a precipitation-strengthened matrix coupled with a metastable cellular austenite network whose stability is tuned into a TRIP-active regime at room temperature. This decoupled microstructure state directly explains why the optimized condition exhibits both high strength and a prolonged uniform work-hardening regime, and it sets the stage for the transformation evidence and stability quantification presented in the following Section.

Stability tailoring and room-temperature TRIP activation

Figure 5 provides combined EBSD and XRD evidence for the stability contrast of reverted austenite between L-600 and TL-480-600[45]: serial *ex-situ* EBSD phase mapping at comparable locations captures the spatial evolution of γ, while XRD quantifies the strain-induced γ → α' transformation[46,47]. In the undeformed state [Figure 5A and E], both conditions contain a high fraction of austenite embedded in a martensitic matrix, with TL-480-600 exhibiting a slightly higher initial austenite fraction[48,49]. Upon loading to 2.5% engineering strain [Figure 5B and F], the two conditions begin to diverge: TL-480-600 shows a more noticeable emergence of deformation-induced martensite within the austenite-containing regions, whereas L-600 remains comparatively austenite-rich, indicating that the austenite in TL-480-600 is more readily activated for γ → α' transformation under room-temperature tension.

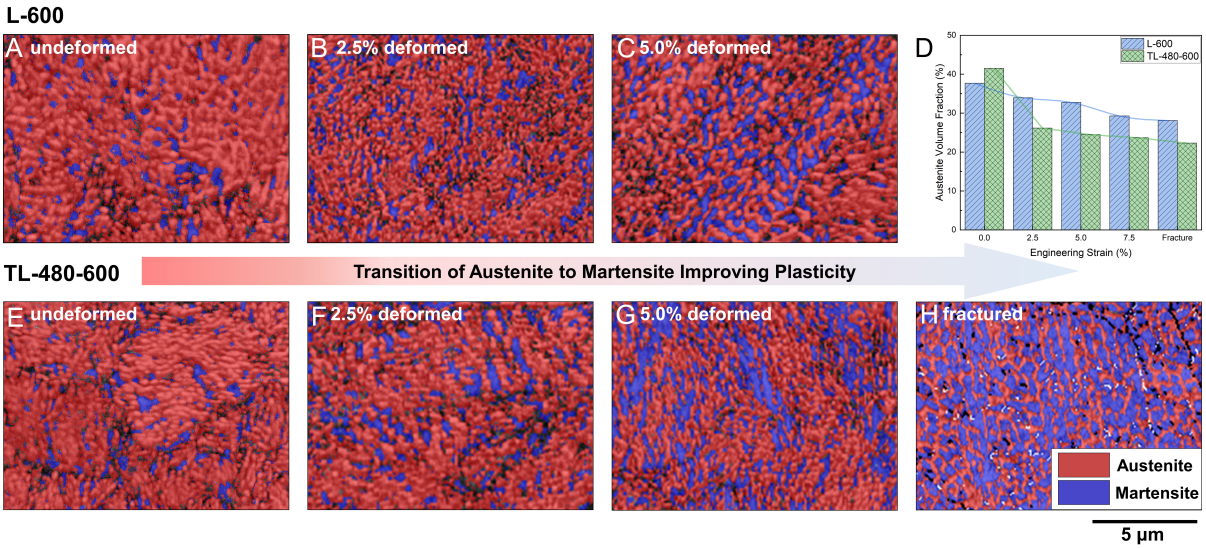

Figure 5. Serial *ex-situ* EBSD phase maps showing deformation-induced γ → α' transformation at room temperature: (A-C) L-600 phase maps at 0%, 2.5% and 5.0% engineering strain; (E-H) TL-480-600 phase maps at 0%, 2.5% and 5.0% engineering strain, and after fracture; (D) Austenite volume fraction as a function of engineering strain measured by XRD. Austenite is shown in red and martensite in blue in the EBSD maps. Scale bar as indicated. EBSD maps were acquired from comparable locations (the same distance from the fracture surface) across strain states. EBSD: Electron backscatter diffraction; XRD: X-ray diffraction.

This difference becomes more pronounced at 5.0% strain [Figure 5C and G]. In TL-480-600, a larger fraction of the initial austenite has transformed into martensite and the transformed regions percolate more extensively, implying a broader TRIP participation across the microstructure. By contrast, L-600 retains a higher fraction of austenite with a less extensive transformation footprint at the same strain, consistent with an over-stabilized austenite state that is difficult to transform at room temperature. Admittedly, the factors governing austenite stability (chemical partitioning and size/morphology) are often interrelated and difficult to decouple in a fully controlled manner. Here, given the comparable austenite fractions [Table 1 and Figure 5D] and broadly similar distribution morphologies between L-600 and TL-480-600 [Figure 5A and E], the different transformation responses revealed by serial *ex-situ* EBSD/XRD lend support to the interpretation that chemical stabilization associated with solute partitioning is a major contributor to the observed stability contrast. After fracture [Figure 5H], the transformed microstructure in TL-480-600 contains substantially more martensite within the mapped regions, confirming that the two-step route enables a larger cumulative martensitic transformation during tensile deformation.

The quantitative evolution is summarized in Figure 5D. The austenite volume fraction in TL-480-600 decreases more steeply (41.5% → 22.3% after fracture) than in L-600 (37.7% → 28.1% after fracture), demonstrating a larger TRIP contribution throughout deformation. This enhanced transformation activity provides a mechanistic explanation for the prolonged strain-hardening regime and the increased uniform elongation observed for TL-480-600: early TRIP activation contributes to high initial hardening and delays localization, while continued transformation at higher strains sustains work hardening over an extended strain window[50].

These observations validate the core stability-tuning concept of this study. The AM-derived cellular segregation tends to stabilize reverted austenite; when over-stabilized (as in L-600), TRIP is suppressed and hardening capacity diminishes earlier. The two-step intercritical strategy, together with the precipitation and partitioning state established in the previous section, shifts the cellular austenite stability into a TRIP-active regime at room temperature, enabling more extensive γ → α' transformation and thereby improving the strength-ductility synergy.

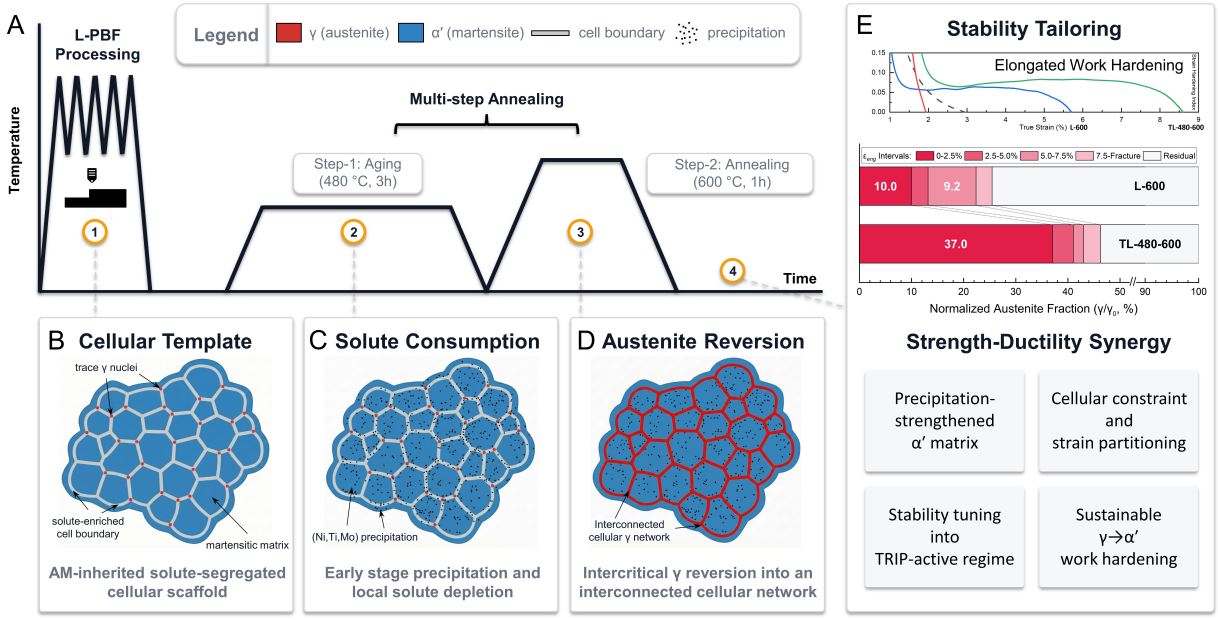

Figure 6. Graphical workflow of the multi-step heat-treatment strategy and the associated microstructure-property relationship: (A) Temperature-time profile for the investigated processing route (480 °C/3 h + 600 °C/1 h); (B-D) Schematic microstructural evolution from the as-printed cellular template through precipitation to intercritical austenite reversion, forming an interconnected austenite network; (E) Stacked bar chart of austenite fraction normalized by the initial austenite fraction (γ/γ_0) across engineering strain intervals. Values are shown for major contributors, minor bins (< 5%) are unlabeled for clarity. AM: Additive manufacturing.

Integrated strengthening-toughening mechanism and design concept

The above results collectively establish an integrated microstructure-property pathway for L-PBF 18Ni300, summarized schematically in Figure 6. Rather than homogenizing the AM-inherited chemical heterogeneity, the optimized multi-step route [Figure 6A] leverages it as a functional template and coordinates precipitation, solute redistribution, austenite reversion, and stability tuning to overcome the conventional strength-ductility trade-off.

As illustrated in Figure 6B, the as-printed cellular framework provides a topological scaffold inherited from rapid solidification, with solute-enriched cell walls serving as preferential sites for subsequent phase reversion. The first aging step (480 °C, 3 h) primarily operates as a solute-consumption stage [Figure 6C], during which nanoscale precipitates form and consume part of the solute reservoir, while the partially retained cellular heterogeneity remains recognizable. This pre-established precipitation and partitioning state becomes critical in the subsequent intercritical annealing step (600 °C, 1 h), where austenite reversion proceeds under the guidance of the cellular template, reconstructing a high-fraction and interconnected reverted-austenite network [Figure 6D]. By reshaping the local solute reservoir near cellular interfaces before and during annealing, the two-step route prevents the reverted austenite from becoming over-stabilized, thereby enabling deliberate stability tailoring into a TRIP-active window. In Figure 6E, the austenite fraction is indicated as a normalized austenite fraction, i.e., γ/γ_0 (normalized by the initial austenite fraction γ_0 for each specimen), to emphasize the relative contribution of each stability interval to the overall strain-hardening response.

Mechanistically, the strength-ductility synergy in TL-480-600 arises from the synergistic contributions of three strengthening/toughening components: (i) precipitation strengthening, which preserves a high-strength martensitic matrix; (ii) cellular-boundary-mediated strengthening and strain partitioning, enabled by the partially retained cellular framework, where mechanically stronger cell-wall regions constrain

the softer cell interiors, thereby promoting strain partitioning and delaying strain localization; and (iii) TRIP-assisted work hardening, achieved by tuning the reverted-austenite stability such that the γ → α' transformation can be sustained during room-temperature tensile deformation. Compared with the single-step intercritical condition (L-600), TL-480-600 exhibits a slightly higher initial austenite fraction (41.5% *vs.* 37.7%), while the primary difference lies in the transformation extent, with a substantially larger strain-induced γ → α' transformation (41.5% → 22.3% *vs.* 37.7% → 28.1%). This increased transformability indicates that the reconstructed austenite network in TL-480-600 is effectively destabilized to participate in tensile deformation via γ → α' transformation, providing a direct microstructural basis for prolonged strain-hardening regime and enhanced uniform deformation (UEL: 7.6% *vs.* 4.7%), which delays strain localization and improves total ductility (TEL: 14.6% *vs.* 9.7%).

A key implication of this integrated mechanism is that for AM maraging steels, simply increasing the reverted-austenite fraction is not adequate because AM-induced solute gradients can over-stabilize cellular austenite and suppress room-temperature TRIP. Thus, the heat-treatment objective should be reconsidered from "maximizing γ" to reconstructing an interconnected γ network and tuning its stability into a desired metastable window[51,52]. Based on the present results, we propose a transferable microstructure design concept of "cellular structure-retained austenite-cellular austenite network", which can be implemented through four practical rules: (i) retain sufficient cellular templating inherited from AM; (ii) reconstruct a percolating reverted-austenite network with high fraction during intercritical annealing; (iii) tailor austenite stability via multi-step heat-treatment design to activate sustained room-temperature TRIP; and (iv) coordinate precipitation strengthening with stability control to achieve strength-ductility synergy. This concept is expected to be extendable to other AM alloys where cellular segregation, metastable phases, and precipitation can be co-designed.

CONCLUSIONS

Cellular austenite reconstruction with a distinct topology. Intercritical processing leverages the AM-inherited cellular segregation template to reconstruct an interconnected cellular austenite network (~40 vol.%).

Multi-step intercritical annealing resolves the "over-stabilized cellular austenite" dilemma. The multi-step strategy reduces excessive austenite stability and enables readily activated room-temperature martensitic TRIP.

Mechanism validation by serial *ex-situ* mapping and transformation quantification. The multi-step condition shows a larger γ → α' transformation than the single-step counterpart, consistent with earlier TRIP activation and prolonged uniform work hardening.

Strength-ductility synergy via an extendable microstructure design concept. The optimized route improves the strength-ductility balance and supports a transferable "cellular template-retained austenite-cellular austenite network" design paradigm for AM metals.

DECLARATIONS

Acknowledgments

The authors would like to thank the Joint Research Center of Additive Manufacturing, School of Materials Science and Engineering, Shanghai Jiao Tong University (SJTU SMSE) – Zhangjiagang, as well as the Instrumental Analysis Center of Shanghai Jiao Tong University (SJTU IAC), for technical support. Shilong Liu sincerely thanks his former mentor, R.D.K. Misra, when he was at the University of Texas at El Paso (UTEP).

Authors' contributions

Conceptualization, investigation, methodology, data acquisition, writing-original draft: Tang, J.; Yu, Y.; Liu,

S.; Jin, X.
Data analysis, technical and material support: Tang, J.; Yu, Y.; Xiong, Z.; Liu, S.
Supervision, project administration, writing-review & editing: Yu, Y.; Xiong, Z.; Liu, S.; Jin, X.; Misra, R. D. K.
Funding acquisition: Yu, Y.; Liu, S.; Jin, X.

Availability of data and materials

The data that support the findings of this study are available from the corresponding authors upon reasonable request.

AI and AI-assisted tools statement

During the preparation of this manuscript, the AI tool ChatGPT (version 5.2, released 2025-12-11) was used solely for language editing. The tool did not influence the study design, data collection, analysis, interpretation, or the scientific content of the work. All authors take full responsibility for the accuracy, integrity, and final content of the manuscript.

Financial support and sponsorship

This work was financially supported by the National Natural Science Foundation of China (Grant No. 52293394, 52501052), the China Postdoctoral Science Foundation (Grant No. 2023M732192), the National Key Laboratory of Science and Technology on Advanced Lightduty Gas-turbine (Grant No. 2023-JJ-18), the Shanghai Explorer Program (Grant No. 25TS1413400), and the Startup Fund for Young Faculty at Shanghai Jiao Tong University (SFYF at SJTU) (Grant No. 25X010502565).

Conflicts of interest

All authors declared that there are no conflicts of interest.

Ethical approval and consent to participate

Not applicable.

Consent for publication

Not applicable.

REFERENCES

1. Herzog, D.; Seyda, V.; Wycisk, E.; Emmelmann, C. Additive manufacturing of metals. *Acta. Mater.* **2016**, *117*, 371-92. DOI
2. Frazier, W. E. Metal additive manufacturing: a review. *J. Mater. Eng. Perform.* **2014**, *23*, 1917-28. DOI
3. Yap, C. Y.; Chua, C. K.; Dong, Z. L.; et al. Review of selective laser melting: materials and applications. *Appl. Phys. Rev.* **2015**, *2*, 041101. DOI
4. Haghdadi, N.; Laleh, M.; Moyle, M.; Primig, S. Additive manufacturing of steels: a review of achievements and challenges. *J. Mater. Sci.* **2020**, *56*, 64-107. DOI
5. Debroy, T.; Wei, H.; Zuback, J.; et al. Additive manufacturing of metallic components - process, structure and properties. *Prog. Mater. Sci.* **2018**, *92*, 112-224. DOI
6. Yan, J.; Zhou, Y.; Gu, R.; Zhang, X.; Quach, W.; Yan, M. A comprehensive study of steel powders (316L, H13, P20 and 18Ni300) for their selective laser melting additive manufacturing. *Metals* **2019**, *9*, 86. DOI
7. Bae, K.; Shin, D.; Kim, J.; Lee, W.; Jo, I.; Lee, J. Influence of post heat treatment condition on corrosion behavior of 18Ni300 maraging steel manufactured by laser powder bed fusion. *Micromachines* **2022**, *13*, 1977. DOI PubMed PMC
8. Song, J.; Tang, Q.; Feng, Q.; et al. Effect of heat treatment on microstructure and mechanical behaviours of 18Ni-300 maraging steel manufactured by selective laser melting. *Opt. Laser. Technol.* **2019**, *120*, 105725. DOI
9. Kempen, K.; Yasa, E.; Thijs, L.; Kruth, J.; Van Humbeeck, J. Microstructure and mechanical properties of selective laser melted 18Ni-300 steel. *Phys. Procedia.* **2011**, *12*, 255-63. DOI

10. Wang, Y.; Zhang, Y.; Gong, W.; et al. On the role of austenite stability in yielding behavior of a medium Mn steel with a duplex austenite-martensite microstructure. *Acta. Mater.* **2025**, *288*, 120840. DOI
11. Yang, L.; Wei, C.; Jiang, F.; et al. Achieving ultrahigh strength and ductility in a Co-Cr-Ni multi-principal element alloy through gradient grain and nanoprecipitate structure. *J. Mater. Sci. Technol.* **2025**, *236*, 262-9. DOI
12. Demir, A. G.; Previtali, B. Investigation of remelting and preheating in SLM of 18Ni300 maraging steel as corrective and preventive measures for porosity reduction. *Int. J. Adv. Manuf. Technol.* **2017**, *93*, 2697-709. DOI
13. Kong, D.; Dong, C.; Wei, S.; et al. About metastable cellular structure in additively manufactured austenitic stainless steels. *Addit. Manuf.* **2021**, *38*, 101804. DOI
14. Sanders, D. J. Temperature distributions produced by scanning Gaussian laser beams. *Appl. Opt.* **1984**, *23*, 30. DOI
15. Casalino, G.; Campanelli, S.; Contuzzi, N.; Ludovico, A. Experimental investigation and statistical optimisation of the selective laser melting process of a maraging steel. *Opt. Laser. Technol.* **2015**, *65*, 151-8. DOI
16. Truong, T.; Asala, G.; Ola, O.; Ojo, O.; Odeshi, A. Effects of additive manufacturing process parameters and heat treatment on texture evolution and variant selection during austenite-martensite transformation in 18%Ni-M350 maraging steel. *Mater. Charact.* **2023**, *204*, 113190. DOI
17. Ronneberg, T.; Davies, C. M.; Hooper, P. A. Revealing relationships between porosity, microstructure and mechanical properties of laser powder bed fusion 316L stainless steel through heat treatment. *Mater. Des.* **2020**, *189*, 108481. DOI
18. Magana-carranza, R.; Sutcliffe, C.; Patterson, E. The effect of processing parameters and material properties on residual forces induced in laser powder bed fusion (L-PBF). *Addit. Manuf.* **2021**, *46*, 102192. DOI
19. Yao, Y.; Fan, L.; Ding, R.; et al. On the role of cellular microstructure in austenite reversion in selective laser melted maraging steel. *J. Mater. Sci. Technol.* **2024**, *184*, 180-94. DOI
20. Kannan, R.; Nandwana, P. Thermodynamics and kinetics of precipitation and austenite reversion during aging of Ti-free grade 300 maraging steel manufactured by laser powder bed fusion (LPBF). *J. Mater. Sci.* **2021**, *56*, 18722-39. DOI
21. Narayana Samy, V. P.; Schäfle, M.; Brasche, F.; Krupp, U.; Haase, C. Understanding the mechanism of columnar–to-equiaxed transition and grain refinement in additively manufactured steel during laser powder bed fusion. *Addit. Manuf.* **2023**, *73*, 103702. DOI
22. Zinsaz-borujerdi, A.; Zarei-hanzaki, A.; Abedi, H.; et al. Room temperature mechanical properties and microstructure of a low alloyed TRIP-assisted steel subjected to one-step and two-step quenching and partitioning process. *Mater. Sci. Eng. A.* **2018**, *725*, 341-9. DOI
23. Dehgahi, S.; Sanjari, M.; Ghoncheh, M.; Amirkhiz, B. S.; Mohammadi, M. Concurrent improvement of strength and ductility in heat-treated C300 maraging steels produced by laser powder bed fusion technique. *Addit. Manuf.* **2021**, *39*, 101847. DOI
24. Conde, F.; Escobar, J.; Oliveira, J.; Jardini, A.; Bose Filho, W.; Avila, J. Austenite reversion kinetics and stability during tempering of an additively manufactured maraging 300 steel. *Addit. Manuf.* **2019**, *29*, 100804. DOI
25. Król, M.; Snopiński, P.; Czech, A. The phase transitions in selective laser-melted 18-NI (300-grade) maraging steel. *J. Therm. Anal. Calorim.* **2020**, *142*, 1011-8. DOI
26. Takata, N.; Ito, Y.; Nishida, R.; Suzuki, A.; Kobashi, M.; Kato, M. Austenite reversion behavior of maraging steel additive-manufactured by laser powder bed fusion. *ISIJ. Int.* **2024**, *64*, 303-15. DOI
27. Strakosova, A.; Roudnická, M.; Šafka, J.; et al. Effect of titanium on microstructure and mechanical behaviour of additively manufactured 1.2709 maraging steel. *Addit. Manuf.* **2024**, *88*, 104264. DOI
28. Jacob, K.; Roy, A.; Gururajan, M.; Jaya, B. N. Effect of dislocation network on precipitate morphology and deformation behaviour in maraging steels: Modelling and experimental validation. *Materialia* **2022**, *21*, 101358. DOI
29. Podgornik, B.; Šinko, M.; Godec, M. Dependence of the wear resistance of additive-manufactured maraging steel on the build direction and heat treatment. *Addit. Manuf.* **2021**, *46*, 102123. DOI
30. Jägle, E. A.; Choi, P.; Van Humbeeck, J.; Raabe, D. Precipitation and austenite reversion behavior of a maraging steel produced by selective laser melting. *J. Mater. Res.* **2014**, *29*, 2072-9. DOI
31. Nandwana, P.; Kannan, R.; Leonard, D. N. Leveraging solute segregation in laser powder bed fusion to achieve superior strength and ductility via single-step heat treatment in Ti-free grade 300 maraging steel. *JOM* **2020**, *72*, 4221-31. DOI
32. He, B. On the factors governing austenite stability: intrinsic versus extrinsic. *Materials* **2020**, *13*, 3440. DOI PubMed PMC
33. Mutua, J.; Nakata, S.; Onda, T.; Chen, Z. Optimization of selective laser melting parameters and influence of post heat treatment on microstructure and mechanical properties of maraging steel. *Mater. Des.* **2018**, *139*, 486-97. DOI
34. Mei, X.; Yan, Y.; Fu, H.; Gao, X.; Huang, S.; Qiao, L. Effect of aging temperature on microstructure evolution and strengthening behavior of L-PBF 18Ni(300) maraging steel. *Addit. Manuf.* **2022**, *58*, 103071. DOI
35. Tekin, T.; Ischia, G.; Naclerio, F.; Ipek, R.; Molinari, A. Effect of a direct aging heat treatment on the microstructure and the tensile properties of a 18Ni-300 maraging steel produced by Laser Powder Bed Fusion. *Mater. Sci. Eng. A.* **2023**, *872*, 144921. DOI
36. Habassi, F.; Houria, M.; Barka, N.; Jahazi, M. Influence of post-treatment on microstructure and mechanical properties of additively manufactured C300 maraging steel. *Mater. Charact.* **2023**, *202*, 112980. DOI

37. He, C.; Yao, H.; Hui, P.; et al. Quasi-in-situ study on the strength-plasticity synergistic mechanism of super martensitic stainless steel with different N content. *Mater. Charact.* **2025**, *229*, 115470. DOI
38. Casati, R.; Lemke, J.; Tuissi, A.; Vedani, M. Aging behaviour and mechanical performance of 18-Ni 300 steel processed by selective laser melting. *Metals* **2016**, *6*, 218. DOI
39. Monkova, K.; Zetkova, I.; Kučerová, L.; Zetek, M.; Monka, P.; Daňa, M. Study of 3D printing direction and effects of heat treatment on mechanical properties of MS1 maraging steel. *Arch. Appl. Mech.* **2018**, *89*, 791-804. DOI
40. Damon, J.; Hanemann, T.; Dietrich, S.; Graf, G.; Lang, K.; Schulze, V. Orientation dependent fatigue performance and mechanisms of selective laser melted maraging steel X3NiCoMoTi18-9-5. *Int. J. Fatigue.* **2019**, *127*, 395-402. DOI
41. Kučerová, L.; Zetková, I.; Jandová, A.; Bystrianský, M. Microstructural characterisation and in-situ straining of additive-manufactured X3NiCoMoTi 18-9-5 maraging steel. *Mater. Sci. Eng. A.* **2019**, *750*, 70-80. DOI
42. Bai, Y.; Yang, Y.; Wang, D.; Zhang, M. Influence mechanism of parameters process and mechanical properties evolution mechanism of maraging steel 300 by selective laser melting. *Mater. Sci. Eng. A.* **2017**, *703*, 116-23. DOI
43. Bajaj, P.; Hariharan, A.; Kini, A.; Kürnsteiner, P.; Raabe, D.; Jägle, E. Steels in additive manufacturing: a review of their microstructure and properties. *Mater. Sci. Eng. A.* **2020**, *772*, 138633. DOI
44. Mohapatra, S.; Poojari, G.; Satpathy, B.; Das, S.; Das, K. A comprehensive study on the effect of annealing temperature on the tensile and impact behavior of automotive-grade medium manganese steel (Fe-6.22Mn-0.18C). *J. Mater. Eng. Perform.* **2023**, *33*, 5348-63. DOI
45. Song, Y.; Li, C.; Liao, Y.; Gu, J. Study on the mechanical stability of reversed austenite in super martensitic stainless steel via in-situ synchrotron high energy X-ray diffraction. *Mater. Lett.* **2023**, *345*, 134495. DOI
46. Han, P.; Liu, Z.; Li, Q.; et al. A phenomenological understanding of the novel design of hierarchical structure for 1 GPa ultrahigh strength and high toughness combination low alloy steel. *Mater. Sci. Eng. A.* **2023**, *881*, 145387. DOI
47. Sahoo, B. K.; Srivastava, V. C.; Mahato, B.; Ghosh Chowdhury, S. Microstructure-mechanical property evaluation and deformation mechanism in Al added medium Mn steel processed through intercritical rolling and annealing. *Mater. Sci. Eng. A.* **2021**, *799*, 140100. DOI
48. Hu, C.; Huang, C.; Liu, Y.; Perlade, A.; Zhu, K.; Huang, M. The dual role of TRIP effect on ductility and toughness of a medium Mn steel. *Acta. Mater.* **2023**, *245*, 118629. DOI
49. Callahan, M.; Hubert, O.; Hild, F.; Perlade, A.; Schmitt, J. Coincidence of strain-induced TRIP and propagative PLC bands in Medium Mn steels. *Mater. Sci. Eng. A.* **2017**, *704*, 391-400. DOI
50. Mao, Z.; Lu, X.; Yang, H.; Niu, X.; Zhang, L.; Xie, X. Processing optimization, microstructure, mechanical properties and nanoprecipitation behavior of 18Ni300 maraging steel in selective laser melting. *Mater. Sci. Eng. A.* **2022**, *830*, 142334. DOI
51. Yadav, M. K.; Kumar, D.; Kumar, N.; Bandyopadhyay, T. K. Hot-rolled Al-added medium Mn steel (Fe-8Mn-2.85Al-1Si-0.2C): Microstructural evolution and tensile behavior. *Materialia* **2023**, *29*, 101790. DOI
52. Suh, D.; Kim, S. Medium Mn transformation-induced plasticity steels: recent progress and challenges. *Scr. Mater.* **2017**, *126*, 63-7. DOI